Excess Path Delays From Sentinel Interferometry to Improve Weather Forecasts

Nazzareno Pierdicca, *Senior Member, IEEE*, Ida Maiello, Eugenio Sansosti, *Senior Member, IEEE*, Giovanna Venuti, Stefano Barindelli, Rossella Ferretti, Andrea Gatti, Mariarosaria Manzo, Andrea Virgilio Monti-Guarnieri, *Senior Member, IEEE*, Federica Murgia, Eugenio Realini, and Simona Verde

***Abstract*—A synthetic aperture radar can offer not only an accurate monitoring of the earth surface deformation, but also information on the troposphere, such as the total path delay or the columnar water vapor at high horizontal resolution. This can be achieved by proper interferometric processing and postprocessing of the radar interferograms. The fine and unprecedented horizontal resolution of the tropospheric products can offer otherwise unattainable information to be assimilated into numerical weather prediction models, which are progressively increasing their resolving capabilities. A number of tricks on the most effective processing approaches, as well as a novel method to pass from multipass differential interferometry products to absolute tropospheric columnar quantities are discussed. The proposed products and methods are assessed using real Sentinel-1 data. The experiment aims at evaluating the accuracy of the derived information and its impact on the weather prediction skill for two meteorological events in Italy. The main perspective of the study is linked to the possibility of exploiting interferometric products from a geosynchronous platform, thus complementing the inherent high resolution of SAR sensors with the required frequent revisit needed for meteorological applications.**

***Index Terms*—Meteorology, numerical weather prediction (NWP), synthetic aperture radar (SAR) interferometry (InSAR), tropospheric path delay, water vapor.**

Manuscript received June 5, 2019; revised December 7, 2019 and March 1, 2020; accepted April 11, 2020. Date of publication May 26, 2020; date of current version June 23, 2020. This work was supported by the Italian Space Agency (ASI) through the SINERGY Project (Synthetic aperture Instrument for Novel Earth Remote-sensed MetereoloGy and IdrologY) under Contract N. 2016-12-U (CUP F82F16001040005). *(Corresponding author: Nazzareno Pierdicca.)*

Nazzareno Pierdicca and Federica Murgia are with the Department of Information Engineering, Electronics and Telecommunications, La Sapienza University of Rome, 00184 Rome, Italy (e-mail: nazzareno.pierdicca@uniroma1.it; federica.murgia@uniroma1.it).

Ida Maiello is with Abruzzo Region, Civil Protection, 67100 L'Aquila, Italy (e-mail: ida.maiello@regione.abruzzo.it).

Eugenio Sansosti, Mariarosaria Manzo, and Simona Verde are with the Institute of Remote Sensing of Environment, National Research Council, 80127 Napoli, Italy (e-mail: eugenio.sansosti@cnr.it; verde.s@irea.cnr.it).

Rossella Ferretti is with the Center of Excellence for Prediction of Severe Events, University of L'Aquila, 67100 L'Aquila, Italy (e-mail: rossella.ferretti@aquila.infn.it).

Andrea Gatti and Eugenio Realini are with the Geomatics Research and Development srl, 22074 Lomazzo, Italy (e-mail: andrea.gatti@g-red.eu; eugenio.realini@g-red.eu).

Giovanna Venuti and Stefano Barindelli are with the Dipartimento di Ingegneria Civile e Ambientale, Politecnico di Milano, 20122 Milano, Italy (e-mail: giovanna.venuti@polimi.it).

Andrea Virgilio Monti-Guarnieri is with the Dipartimento di Elettronica, Informazione e Bioingegneria, Politecnico di Milano, 20122 Milano, Italy (e-mail: andrea.montiguarnieri@polimi.it).

Digital Object Identifier 10.1109/JSTARS.2020.2988724

I. Introduction

THE violence and frequency of extreme weather events are increasing. Improving the weather forecast accuracy is a fundamental goal to limit their social and economic damage. Indeed, numerical weather prediction (NWP) models are improving their capability to provide a high-resolution description of the atmosphere. The large growth of computational resources in the past decades has enabled NWP models to provide a high-resolution description of the atmosphere at regional scale and a better description of key physical processes, such as radiative transfer, microphysics, and planetary boundary layer. Nonhydrostatic limited-area atmospheric prediction systems are capable of modeling a variety of physical processes by different parameterization schemes down to horizontal resolution of the order of 1 km [1]. Large-eddy simulation (LES) models provide a detailed description of the turbulence and can reach resolution potentially down to a few hundreds of meters [2]. Consequently, it is increasing the need to collect data to initialize the model and/or to be assimilated at a suitable resolution in space.

Satellite remote sensing can offer such kind of data regarding both the earth's surface and the atmosphere. An emerging technique in this field is the synthetic aperture radar (SAR) interferometry (InSAR). InSAR is largely exploited to derive accurate digital elevation models (DEM) or to measure the earth surface displacement in time with a precision in the order of centimeters. This is achieved by measuring the difference in phase of the radar echo collected from different viewpoints and/or at different times. This measurement is generally hampered by several errors—geometric inaccuracies (orbital information and/or DEM errors), spatial and temporal decorrelation effects, processing issues (mainly phase unwrapping errors), and atmospheric effects [3]. The latter effects, which are particularly relevant to the topic of this article, introduce an additional phase difference, usually referred to as atmospheric phase screen (APS). This difference is due to changes in the tropospheric composition, which introduce a bending of the electromagnetic wave path and modifies the wave propagation velocity [4]. This can be misinterpreted as an additional surface deformation or can lead to an error in DEM retrieval. Correcting tropospheric effects is a major problem for ordinary InSAR applications. Modern InSAR techniques are based on multipass SAR data [5], [6]. Among other advantages, they provide a good sampling of the APS spatial-temporal variability, enabling to some extent to

distinguish the spatially correlated atmospheric signal from the temporally correlated deformation signal by suitable statistical filtering.

Although often treated as noise, the APS can be turned into useful information for meteorologists if the DEM is known and deformations are absent or can be modeled [3]. Considering that meteorological applications generally require very frequent observations, a SAR on a geosynchronous orbit would represent a breakthrough in this respect [7]. It would be capable to produce high spatial resolution APS and tropospheric path delay maps with high temporal revisit (hours or less) to be assimilated into NWP models. A geosynchronous SAR mission, named G-CLASS (geosynchronous continental land-atmosphere sensing system), has been recently selected by the European Space Agency (ESA) in response to the call for a future Earth Explore satellite (EE-10).

The exploitation of InSAR as a meteorological tool providing high spatial resolution precipitable water vapor (PWV) or zenith total delay (ZTD) through the troposphere is not new. There are advantages with respect to alternative techniques, as radiosondes are launched from few sites and at synoptic hours only, global navigation satellite system (GNSS) receiver networks are generally too sparse, microwave radiometers have poor spatial resolution, and near infrared radiometers work only at daytime and are affected by cloud cover.

Pioneer studies deriving PWV or ZTD from APS and assessing their impacts on NWP skill were published in the past [8]–[15]. Very recent papers are [16]–[18]. It must be considered that InSAR is an inherently differential technique that provides difference in time of PWV or ZTD referred to an unknown point on the earth (acting as a bias) and that additional factors may affect the phase difference and must be removed [3]. Ancillary and prior information are needed to remove the unwanted effects and to convert the differential information into absolute values of the columnar tropospheric quantities (i.e., PWV or ZTD) required by NWP assimilation.

In the literature, strategies to remove the unwanted factors (e.g., error in spatial baseline determination, unknown bias term) and calibrate the APSs are proposed. Specifically, if a suitable network of GNSS receivers is available in the area and provides pointwise values of PWV or ZTD, it can be effectively exploited [15]. Estimation of a factor in the APS associated to changes in the atmospheric stratification can be done by fitting a suitable function of the earth surface height [11]. Removal of surface motion contribution to APS maps is sometime carried out by spatial–temporal filtering techniques based on the assumption that the APS signal is highly correlated in space and poorly correlated in time [5], [6]. The latter two approaches must be applied with care if the final objective is the retrieval of tropospheric quantities. In fact, the estimation of a unique stratification term as a function of surface height can be nonrealistic, as it will be discussed later. In addition, spatial–temporal filtering can remove atmospheric signal if the latter has signatures comparable to other geophysical quantities (e.g., surface deformations). In order to convert the differential information into an absolute one, different approaches have been carried out. In [15], the authors assume that the atmospheric state is known at a certain time (e.g., the time of the first SAR acquisition); Alshawaf *et al.* consider that the temporal mean of the columnar parameter is constant in the considered area [11]; Pichelli *et al.* assume that another spaceborne sensor provides the temporal mean [10]. In [16], the retrieval of a time sequence of PWV maps is proposed, with the first map of the sequence provided by the ERA-Interim model and subsequent interferometric pairs calibrated using GNSS receivers. All these assumptions have pro and cons. They could be too approximated (i.e., assuming a constant mean or a known reference atmosphere at a certain epoch), lose some atmospheric signals (i.e., applying spatial–temporal filters), or not feasible (e.g., the presence of an alternative sensor, such as a near infrared radiometer, is not always guaranteed on the same platform).

This article presents a preparatory work in view of a future geosynchronous SAR to propose and assess methods to derive absolute troposphere columnar quantities. The approach reported here is founded on a multipass InSAR technique to estimate the APSs. This means that the APSs are not derived from a single pair of images but are retrieved from a long stack of SAR acquisitions paired in different ways to form a large number of interferograms. Consistently, it assimilates GNSS observations into the NWP model, which is run continuously in parallel to the acquisition of the SAR data stack, in order to retrieve the temporal mean needed to get the absolute values. This is a major novelty of the proposed approach. Additionally, most of the previous works assimilate the PWV by removing the dry component of the path delay predicted by the NWP model. Here, we assimilate the total delay, as suggested in [19], since the APS*s* are shown to bring important information not only on the water vapor, but also on the vertical stratification of the atmosphere that determines the relationship between the path delay and the surface height. As far as the calibration of the APSs is concerned, we resort on a GNSS receiver network, as in the literature, but we propose a method to join the station with the SAR APS over areas with complex topography.

The experimental part of the work considers Sentinel-1 data and assesses their impact on the forecasting skill of a local-area NWP model. We consider the advanced research WRF (ARW) modeling system, developed at the National Center for Atmospheric Research (NCAR) laboratories and assimilate the ZTD derived from a GNSS receiver network and from InSAR APS maps using a 3-D variational (3D-Var) assimilation scheme. The results of the assimilation are compared to surface observations of rain rate and brightness temperature measured by a ground-based radiometer. Two different precipitation events that occurred in Northern Italy over the Po valley are considered; the precipitation rate is predicted with and without the assimilation, and the results are compared to the one measured on ground. Results indicate the potential of InSAR as a meteorological tool.

The rest of this article is organized as follows. Section II introduces the main equations relating the interferometric phase to tropospheric variables. It also reviews the two case studies considered for the experiment and the methods exploited to process the Sentinel-1 and GNSS data. Section III details the steps carried out to convert InSAR APS*s* into absolute maps of troposphere columnar quantities. The validation of the maps is also reported. Section IV describes the adopted NWP model and the data assimilation

(DA) approach. It also evaluates the forecasting skill when assimilating the GNSS and InSAR derived ZTD maps. Section V draws the conclusions of this article.

II. Data and Methods

A. Atmospheric Phase Screen

In this work we use a multipass InSAR approach. In this case, *M*+1 SAR images are properly combined to obtain a time series of *M* interferometric phases. There exist several possible approaches for computing such time series [20]. Independent of the particular approach, each point in the *i*th element of the time series represents a double difference: 1) a time difference of the phase of the radar echo between the *i*th acquisition and a reference one (usually the first one, which we will refer to as the *master*) and 2) a spatial difference since phase measurements are referred to the phase of a fixed point, arbitrarily chosen within the SAR image. Therefore, at the discrete time *i* (i.e., at the time of acquisition of the *i*th image), the interferometric phase at the image point with range and azimuth coordinates (r, x) is

$$\psi_i\ (r,x) = \phi_i\,(r,x) - \phi_m\,(r,x) - [\phi_i\,(r_0,x_0) - \phi_m\,(r_0,x_0)] \quad i\ =\ 1,\ldots,M \tag{1}$$

where $\phi_i(x,r)$ is the (absolute) phase of the *i*th SAR acquisition, (r_0, x_0) is the arbitrary reference point position, and the subscript *m* indicates the reference acquisition (i.e., the master). The phase ψ is the measurement that is accessible through the InSAR technique. It depends on surface topography (*topo*), a "flat surface" component (*flat*), the surface displacements (*displ*), and the atmosphere temporal changes expressed as a function of the difference in path delay ΔL_{atmo}. If we consider an additional error $v(r,x)$ (e.g., thermal random noise) and the fact that the term in square brackets in (1) can be represented as an unknown constant c_i, the following equation holds:

$$\psi_i\ (r,x) = \Delta\phi_{\mathrm{displ}}\,(r,x) + \Delta\phi_{\mathrm{topo}}\,(r,x) + \Delta\phi_{\mathrm{flat}}\,(r,x) + \frac{4\pi}{\lambda}\left[\Delta L_{\mathrm{atmo}}\,(r,x) + c_i + v\,(r,x)\right] \tag{2}$$

where the bias c_i and the error are expressed in path delay units. For a steady surface (or a surface with known displacement), after removing *topo*, *flat*, and *displ* contributions and after performing the phase unwrapping, [21], [22], we get the delay difference, known as APS of the *i*th acquisition with respect to the master, which, according to our notation, is given by

$$\mathrm{APS}_i\ (r,x) = \frac{\lambda}{4\pi}\,\psi_i\ (r,x) = L_i\ (r,x) - L_m\,(r,x) + c_i + v\,(r,x) \tag{3}$$

We note that, due to the side-looking geometry of SAR systems, the path delay in (3) is along the radar line of sight (LOS), i.e., it represents a slant total delay (STD). On the other hand, the path delay is usually considered in the vertical direction, namely, the ZTD, so that a suitable mapping function must be applied when combining GNSS and InSAR observations.

The path delay is equal to the integral of the atmospheric refractivity along the LOS, which includes the troposphere and the ionosphere. As for C- and X-Band systems, the ionosphere introduces mainly planar phase components in the interferograms [23]. The spatially variable APS is, therefore, due essentially to the troposphere. The total tropospheric delay can be divided into the hydrostatic term, caused primarily by dry gases in the atmosphere, and the wet term, caused by refractivity variation due to the water vapor, i.e., $\mathrm{ZTD}\ =\ \mathrm{ZHD} + \mathrm{ZWD}$ [4].

The wet components of the zenith path delay, considering the atmospheric pressure as the integrand variable, is [24]

$$\mathrm{ZWD}\ = 10^{-6}\ \int_0^{p_s} q\,(p)\left(k' + \frac{k_3}{T\,(p)}\right)\frac{R_d}{g_s\,(\varphi)\,\varepsilon}dp \tag{4}$$

where q is the specific humidity, T is the temperature, p is the pressure, and g_s is the gravitational acceleration at the surface as function of latitude ϕ. The upper limit p_s is the pressure at the surface, R_d is the gas constant for dry air, and $\varepsilon = 0.66$. For the constants, we use $k^{'} = 2.21\ 10^{-7}$ K/Pa and $k_3 = 3.7\ 10^{-3}$ K^2/Pa [25]. The dry component can be accurately approximated by using the surface quantities only, through the following formula [24]:

$$\mathrm{ZHD}\ = 10^{-6}\ \int_0^{p_s} k_1\frac{R}{g_s\,(\varphi)}dp \cong 2.2768\ 10^{-5}\ \left[\frac{m}{Pa}\right]\frac{p_s}{z_f} \tag{5}$$

with $z_f\ =\ 1 - 2.6610^{-3}\cos\cos\,(2)\ - 2.8\ 10^{-7}[m^{-1}]h_a,\ h_a$ being the surface height.

ZWD is approximately proportional to the PWV, the latter being generally in the range between 0.4 and 4.5 cm [10]. The following approximated relation holds [25]:

$$ZWD = 10^{-6}\,(k_3/T_m + k')\,R_v\rho_v PWV \sim 6.4PWV\ [m] \tag{6}$$

where R_v is the gas constant for water vapor, $\rho_v\ =\ 1000$ kg m^{-3}, and T_m is the mean temperature of water vapor along the path. Thus, the InSAR technique is capable of measuring along a slant path $\mathrm{APS}\ =\ \Delta\ L_{\mathrm{atmo}} =\ \Delta\mathrm{STD}$, and thus to furnish the water vapor integrated along that path by removing the dry component.

The differential STD (ΔSTD) can be correlated to the terrain height, either positively or negatively, depending on the atmosphere stratification, e.g., the diverse vertical distribution of atmospheric parameters when the two images were acquired. This stratification term is sometimes distinguished by the turbulent term of the APS map and estimated separately from GNSS data, as discussed in Section I [11].

In conclusion, the APS must be first calibrated to correct for the unknown constant and, as will be discussed later, for other artifacts embedded in the *v(r,x)* error term, and then, converted from differential to absolute value to provide the final delay ZTD or integrated water vapor PWV to be assimilated into an NWP model. The methodological aspects of this work, as well as the data used for validating the approach are described in the following sections.

B. Case Studies

Two experiments were carried out to investigate the impact of the assimilation of GNSS and Sentinel-1 data on the precipitation forecasted by an NWP model. We selected a predominantly flat area (in order to minimize the influence of topography in the

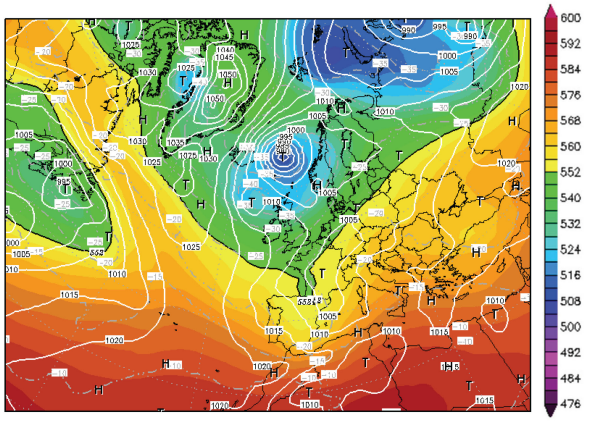

Fig. 1. Case 1 on 27th April 2015. 500 hPa geopotential height (gpdm), temperature (°C), and mean sea level pressure (hPa) at 00 UTC of 27th April. Sentinel-1 overpass occurred on 27th April at UTC 05:24:30. *Source http://www.wetterzentrale.de/*.

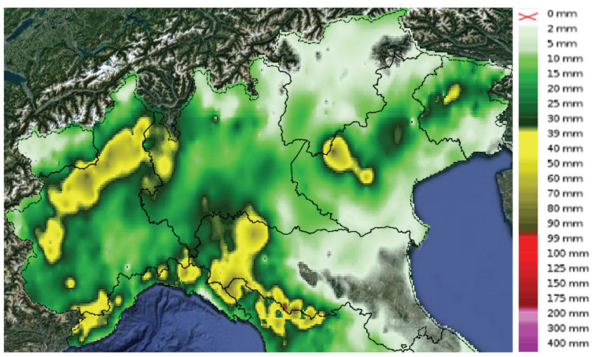

Fig. 2. Twelve-hour accumulated rainfall from 06 UTC to 18 UTC of 27th April 2015. Black contours represent the Italian regions' boundaries. Source DEWETRA platform, a courtesy of the Italian Civil Protection Department.

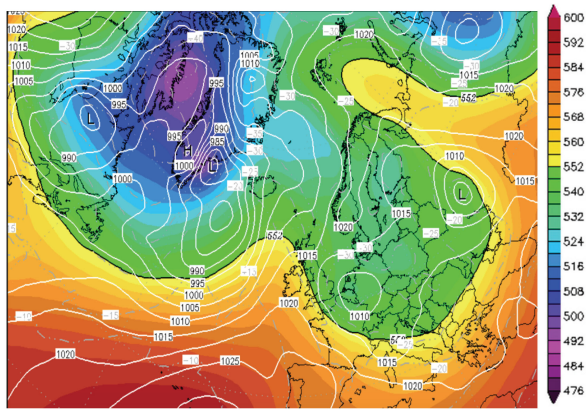

Fig. 3. Case 2 on 11th November 2016. 500 hPa geopotential height (gpdm), temperature (°C), and mean sea level pressure (hPa) at 00 UTC of 11th November. Sentinel-1 overpass occurred on 11th November at UTC 05:19:09. *Source http://www.wetterzentrale.de/*.

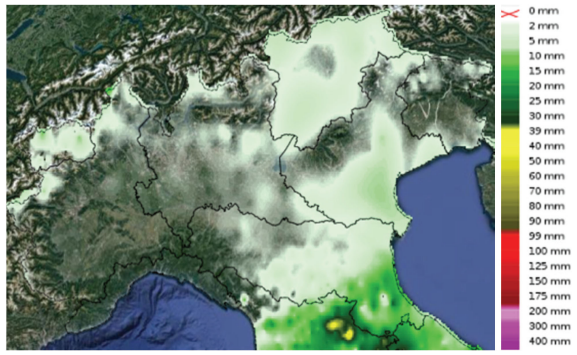

Fig. 4. Twelve-hour accumulated rainfall from 06 UTC to 18 UTC of 11th November 2016. Black contours represent the Italian regions' boundaries. Source DEWETRA platform, a courtesy of the Italian Civil Protection Department.

interferograms), where a long sequence of Sentinel-1 acquisitions was available to run the InSAR multipass technique. Moreover, we checked the availability of data to calibrate/validate the APS maps, to run the model and to validate its results. We also looked for events not too late from the previous Sentinel-1 overpass in order to ensure an impact of SAR assimilation into the model The Northern Italian area and the Sentinel-1 relative orbit number 168 (descending) covering the Po Valley were finally chosen. In that area, two meteorological events (one in Spring and the other in Autumn) were identified as suitable for the assimilation experiments, i.e., on 27th April 2015 (case study 1) and 11th November 2016 (case study 2). A weather synopsis is provided hereafter for each event.

As for case study 1, north of the Alps, a cold front entered Germany from the northwest and sharpened during the afternoon, spanning SW-E across Germany with a convergence line on its warm side and a low-pressure core over south-eastern Germany (see Fig. 1). In the next day, a surface low developed over Central Italy (not shown). This structure was associated with precipitation occurring mostly in northern Italy during the first day.

In Fig. 2, the 12-h accumulated rainfall from 06 UTC of 27th April 2015 shows peaks of accumulated precipitation reaching 80 mm in the northwest side of the Po Valley; similarly, a cell smaller than the previous one is found in the northeast. The map is derived from the rain gauge network (approximately 3800 stations all over Italy) of the Italian Civil Protection Department (DPC) through the DEWETRA© web-GIS by DPC and CIMA Research Foundation. Rain rate were spatially interpolated using a kriging approach available on DEWETRA [26]. In the imaged area, rain gauge stations have an average separation of about 11 km.

Regarding case study 2, a deep intrusion of cold air associated with a Rossby wave elongated from Scandinavia (see Fig. 3) was moving over a still warm Adriatic Sea in the following 24 h (not shown). A surface low developed over central Italy, advecting warm and humid air from southwest and allowing for precipitation to occur.

In Fig. 4, 12-h accumulated rainfall from 06 UTC of 11th November 2016, obtained from the Italian rain gauge network, shows moderate rainfall in central Italy and light precipitation in the eastside of the Po Valley.

C. Sentinel-1 SAR Data and Processing

The Sentinel-1 data acquired in interferometric wide-swath mode (IW) along descending orbit 168 cover the main area of the selected events (see Fig. 5). The data were processed by

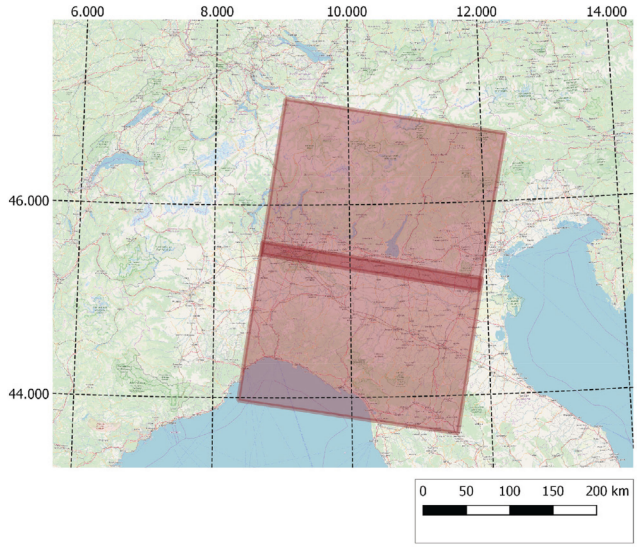

Fig. 5. Sentinel-1 frames considered in this work. As for relative orbit number 168, two different frames had to be combined in order to cover the area of interest.

using an implementation of the small baseline subset (SBAS) technique, known as P-SBAS (see [6]), that works unsupervised on parallel architecture [27], [28]. The SBAS algorithm makes use of multilook operation while generating a set of small baseline interferograms; data are spatially averaged, thus reducing the final spatial resolution. Moreover, the use of only small temporal/perpendicular baseline pairs allows to drastically mitigate the phase decorrelation noise.

Along the selected orbit, the area of interest is covered by two contiguous frames, named N2 (the most northerly) and N3 (the most southerly). Unfortunately, neither frames were acquired along all the orbital passes in the IW mode. We found 59 SAR images between 22/03/2015 and 29/03/2017 for the N2 frame, while 67 images were acquired between 22/03/2015 and 05/03/2017 for the N3 frame. Some of the acquisitions of the N2 frame were not acquired/available on the N3 one, and vice versa, resulting in only 54 images common to the two frames between 22/03/2015 and 22/02/2017. For this reason, and to maximize both the spatial and temporal coverage, the two frames were processed separately and subsequently joined.

We generated a set of 145 small baseline interferograms for the N2 frame. In this case, the effective revisit time is almost constantly 12 days; in only three cases, it rises to 24 days and only one to 32. Only three Sentinel-1B images are available.

For the N3 frame, we generated a set of 164 small baseline interferograms. The effective revisit time is almost constantly 12 days until 24/09/2016, when it becomes 6 days thanks to the addition of Sentinel-1B data. In only two cases, before October 2016, it increases to 24 days and only once to 32 days, while after October 2016, it increases to 12 days only twice. Variations of the effective revisit time take place because the corresponding acquisitions were either unavailable or discarded by the processing procedure.

Overall, a spatial multilook operation implemented through a 5×20 pixels (azimuth/range) average window was carried out for the generation of the interferograms, thus resulting in a final pixel size of about 70 m in both directions. No spatial–temporal

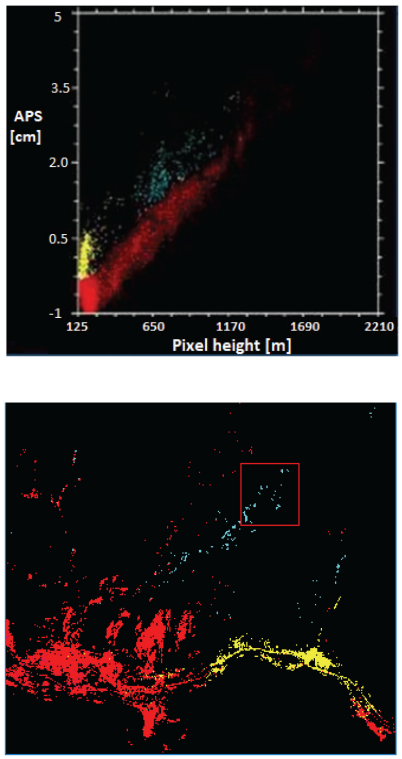

Fig. 6. Upper panel: Plot of the APS as function of the surface height provided by the SRTM DEM. Bottom panel: Map of APS in the considered region. Colors identify different trends with height in both panels and shows that different trends are distinctive of different areas in the image.

filter was applied to the stack to avoid removing atmospheric signals.

An error in the interferograms derives from the nonperfect knowledge of the satellite orbital position. This information is necessary to compensate for the phase contribution of topography and flat earth. It can be demonstrated that, although to the first-order approximation, this artifact is essentially a linear ramp in range and/or azimuth [29]. A similar linear trend is due to the ionosphere. A current processing strategy consists of either correcting the orbits until this ramp contribution is minimized [29], or by simply fitting a ramp to the data and remove it. As mentioned in Section I, phase ramp components in the data may be associated with tropospheric contributions too. For instance, an altitude increase in one direction produces a phase ramp in that direction due to the correlation between APS and height discussed in Section II-A. Clearly, when the goal of the processing is the measurement of ground deformation, it is important just to remove those ramps, not to correctly attribute them to orbital or atmospheric artifacts. On the other hand, when the objective is the APS generation, those ramp removal strategies can impair the estimation of the atmospheric phase signal. For this reason, we chose to handle the orbital ramp removal with the help of external data, namely GNSS, as described in Section III-A.

A deeper investigation of this issue is worth to be carried out. Upper plot of Fig. 6 presents an example of APS's as function of the surface height in a region of the considered Sentinel-1 frame characterized by a rough topography. We can see that different clouds of points are present, with different

Fig. 7. GNSS ground receivers used for APS calibration. In yellow, the stations working only on 27th April 2015; in green, those working only on November 11th, 2016; in red, those working on both dates.

slopes. Those different slopes can be recognized pertaining to different areas in the image, typically different valleys. This shows that considering a unique trend of APS versus height can be a very rough approximation, although it is often adopted. It can be suitable when the objective is removing the effect of atmospheric stratification on the displacement maps in standard InSAR applications. However, it can be detrimental when using InSAR for meteorological applications as in this work. We risk removing the information about atmospheric stratification and its horizontal spatial variability brought by SAR.

Finally, we notice that in other works (e.g., [15]) the wet component of the delay or the PWV are assimilated and the dry component, mostly responsible of the stratification contribution, is removed based on the same NWP model outcomes. Based on the above-mentioned observations, in our work, we assimilate the total tropospheric delay rather than the wet component for the purpose of retaining the information on the vertical stratification and its variability.

D. GNSS Network and Data Processing

Estimates of ZTD from GNSS (from now on named GNSS-ZTD) are used here to calibrate and validate the APS maps and to convert differential InSAR slant delays into absolute zenith delays (see Sections III-A and III-B). Although 85 GNSS permanent stations were present in the test area, only 20% of them could be used, due to lack of observations simultaneous to the selected Sentinel-1 overpasses (see Fig. 7). This percentage was even lower for the first five overpasses, when the stations operated by Lombardia region were switched off. For each acquisition date of the InSAR image stack, two days of raw data at a 30-s rate were collected and processed, using the free and open source goGPS software [30], [31]. Time series of ZTD were obtained by applying a precise point positioning (PPP) strategy to GPS only iono-free combinations of dual-frequency phase observations [32]. The satellite cutoff was set to 10° and the global mapping function was used to project STDs onto the zenith direction; tropospheric gradients were not estimated; the models for antenna phase centers, for solid earth tides and for ocean loading are those used in [33]. The Kalman filter solution strategy was used, by fixing the station coordinate parameters and modeling the receiver clock and ZTD parameters as random walk processes [32]. The standard deviation of the receiver clock increments was set to a large value to account for their unpredictable behavior, while that of the ZTD increments was set to $1\sqrt{\Delta t}(mm/\sqrt{h})$, where Δt is the 30-s processing rate, expressed in hours.

An assessment of the GNSS estimates was preliminarily performed against the data of four radiosonde stations: Milano-Linate, Cuneo-Savigliano, Ferrara-San Pietro Capofiume, and Udine-Rivolto (see Fig. 7). The comparison was performed in terms of ZTD, integrating both (4) and (5) by a simple trapezoidal rule. A correction term was applied to account for the height offset between the GNSS and the radiosonde stations. This was computed as the difference of the ZTD values of the compared stations as derived from the Saastamoinen model. The standard deviation of the differences between ZTDs derived from radiosondes and those of the closest GNSS station was below 1.2 cm for all the four considered stations.

III. Absolute Path Delay

A. APS Calibration Using the GNSS Receiver Network

As explained in Section II-A, each APS is defined but for a constant c_i. Moreover, it may contain a linear trend as a function of the image coordinates (r, x), due to errors in the knowledge of satellite orbits and to the ionosphere [29]. Overall, the error $v(r, x)$ in (3) can be split into a deterministic part and a residual random noise ε, i.e., $v(r,x) = \alpha + \beta r + \gamma x + \varepsilon(r, x)$. The APS calibration consists in the estimation and removal of this deterministic part, as well as the constant term c_i, which cannot be separated by the constant value α. Since a linear function best fitting the APSs themselves can contain atmospheric signals, as already discussed, the calibration must be performed by fitting the residuals between the uncalibrated APSs and the corrected values derived from an independent source in at least three different points. The corrected values can be derived from GNSS-ZTDs of stations falling in the imaged area and simultaneous to the APS slave and master epochs, properly projected onto the LOS. For each APS_i, N simultaneous GNSS slant delay time differences were computed, one for each station k ($k = 1, \ldots, N$) in the imaged area

$$\mathrm{APS}_i^{\mathrm{GNSS}_k} = \frac{\mathrm{ZTD}_i^k - \mathrm{ZTD}_m^k}{\cos\theta^{\,k}} \tag{7}$$

where $\cos\theta^{\,k}$ is the zenith direction of the SAR LOS in the position of the station k. The following set of N observation equations can then be written for each epoch i:

$$\mathrm{APS}_i^{\mathrm{SAR}}(r_k, x_k) - \mathrm{APS}_i^{\mathrm{GNSS}_k} = (\alpha_i + c_i) + \beta_i r_k + \gamma_i x_k + \varepsilon_i^k = \alpha_i' + \beta_i r_k + \gamma_i x_k + \varepsilon_i^k. \tag{8}$$

Once the parameters were estimated by a least square approach, the corresponding planes were removed from SAR APSs to accomplish the calibration. The overall procedure is schematically depicted in Fig. 8.

The calibration procedure was performed on the stack of 59 APS maps related to relative orbit 168, by deriving a common

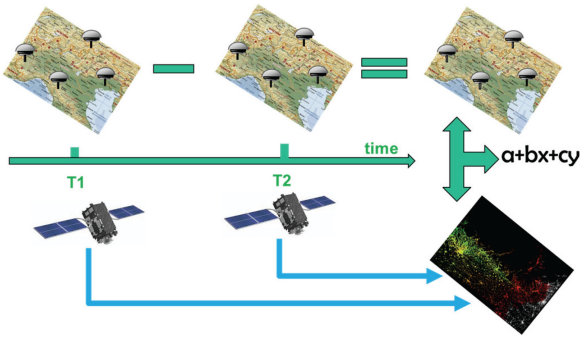

Fig. 8. Schematic view of the APS map calibration process using absolute pointwise ZTD estimates from GNSS at the time of slave t_2 and master t_1 acquisitions. The difference in ZTD from GNSS (upper part) is projected into the LOS and compared to the APS derived from SAR at time t_2 and t_1 (lower part) to fit a bilinear function.

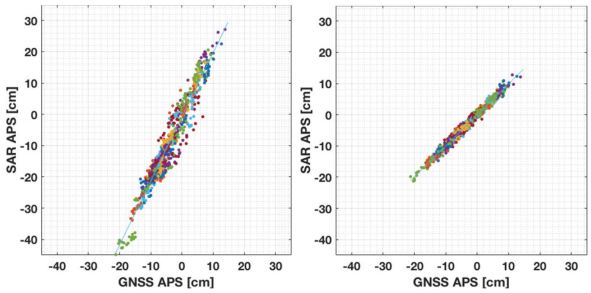

Fig. 9. Scatterplot of Sentinel-1 APS at the GNSS station location versus the GNSS-ZTD time differences (both differential quantities) before (left) and after (right) APS map calibration. Colors refer to different epochs.

calibration plane for both frames N2 and N3. Fig. 9 shows the comparison between the SAR APS*s* and the GNSS derived APSs before and after the calibration process. After calibration, the two APS values agree within 1.2 cm in terms of the standard deviation of differences, which corresponds approximately to 1.8 mm of PWV.

This approach is similar to what is described, e.g., in [15] and [16], with the difference that here we are retrieving the plane in the range/azimuth coordinates. More notably, we combined GNSS and APS values on the bases of the following considerations, which are relevant in areas with complex topography.

At a given epoch, each GNSS-ZTD value is the estimated common zenith component of the slant delays affecting the signals collected from all satellites simultaneously in view. This means that the ZTD is associated to an overturned cone stemming from the GNSS station with semiaperture equal to $90°-\alpha$, α being the GNSS elevation cutoff. Instead, the SAR APS accounts for the delay along the LOS. To account for this discrepancy, usually a local mean of the SAR APS values is computed and then compared to GNSS-ZTD [34]. This approach, however, can introduce errors in mountainous areas. As stated at the end of Section II-C, a local and spatially variable linear trend of the APS with height might be present. As the simple space average could mix pixels at different heights, this would lead to a wrong comparison with the GNSS value. For this reason, in our approach, a regression line of APSs belonging to an area of 1.5 km around each GNSS station as a function of their height was first estimated. The APS value for the comparison was then

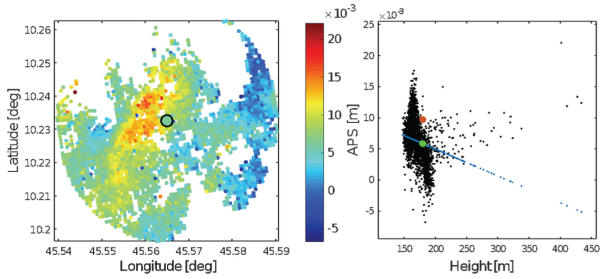

Fig. 10. Left panel: Map of APS*s* in a 1.5-km radius mountainous area around a GNSS station. Right panel: APS trend as a function of height and estimated regression line. Green and red dots are the APS value combined with the GNSS station (at about 180 m elevation) and the APS of the pixel closest to the station, respectively.

selected as the value belonging to this line corresponding to the GNSS station height. Fig. 10, left panel, shows an example of the area surrounding a GNSS station located in a mountainous region, with all the available pixels within a 1.5-km radius color coded according to the APS value. The local behavior of the APSs as function of height is shown in the right panel of the figure, together with the estimated regression line. The final APS value used in the comparison (green dot) and the one of the closest pixel (red dot) exhibit a difference of about 5 mm in this case.

B. From APS to the Absolute Path Delay

For the purpose of DA into NWP models, we need the absolute delay at the epoch of the assimilation, i.e., the quantity $L_i(r,x)$ in (3). This implies the knowledge of the absolute delay at the master epoch, based on some reference data, i.e., $L_m^{\mathrm{REF}}(r,\ x)$. In the literature, the most followed approach assumes the knowledge of the master atmosphere based on the output of a meteorological model eventually tuned by assimilating ancillary data such as GNSS retrievals of ZTD (from now on named GNSS-ZTD) [15]. Assuming that the calibration step has removed the unknown bias and the orbital plane, denoting the random error affecting the master with $\varepsilon^{\mathrm{REF}}$, the following holds for the estimated atmosphere:

$$\tilde{L}_i\ (r,x) = \mathrm{APS}_i\,(r,x) + L_m^{\mathrm{REF}}\ (r,x) + \varepsilon^{\mathrm{REF}}\,(r,x)\,. \quad (9)$$

The error in the master atmosphere is eventually combined with the residual (i.e., after removing the bias and the orbital plane) random error in the APS estimates.

Here, we proceed as already proposed in [10], i.e., we consider the expected values (denoted by an overbar) of the APS and the atmospheric path delay. The SAR image stack, processed according to the multipass InSAR technique, provides the expected value of APSs, whereas a reference source is assumed to provide the expected value of the tropospheric delay, rather than assuming it constant as done, for instance, in [11]. Therefore, we get for the estimated delay at the time of the slave acquisition

$$\tilde{L}_i\ (r,x) = \ \mathrm{APS}i\,(r,x) + \overline{L(r,x)^{\mathrm{REF}}} - \overline{\mathrm{APS}\,(r,x)} - \overline{\varepsilon(r,x)^{\mathrm{REF}}}. \quad (10)$$

Using this approach, the error is now the one associated with the mean tropospheric delay derived from the reference

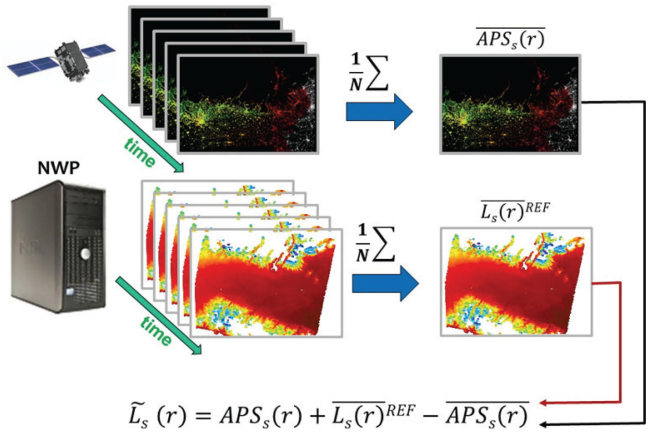

Fig. 11. Schematic view of the process to convert the differential APS into absolute ZTD (SAR-ZTD) using a reference "mean" derived by routinely running the NWP model.

source, which is much lower than that of the individual master atmosphere if the number of averaged samples is high. Assuming statistically independent errors, the standard deviation is reduced by the square root of the number of averaged samples.

In [10], Pichelli *et al.* did a similar experiment using the advance SAR (ASAR) Envisat data and assimilating the PWV after removing the dry component of the ZTD. They used the PWV from MERIS instrument as the reference for computing the mean troposphere, which was available over the same satellite platform and collected at the same time of the ASAR data. Since on board Sentinel-1 there is not such an instrument and in order to design an approach feasible using satellite data only from SAR, here we propose to use the NWP model itself to build the average $\overline{L(r,x)}^{\mathrm{REF}}$. The approach can be easily implemented in an operational weather forecast service at a regional scale that foresees the continuous run of the NWP model. In our case, we run the 3D-Var module assimilating the ZTD retrieved from GNSS at each Sentinel-1 overpass. In other words, the assimilation procedure (specifically the 3D-Var discussed in Section IV-A) was used as a sort of "physical interpolator" of the GNSS-ZTDs to provide a stack of modeled atmospheric delay maps to be averaged.

Fig. 11 provides a schematic overview of the two pipelines that process the SAR acquisitions and run the NWP assimilation module, respectively, to derive both APS and path delay averages.

The data flow of the overall procedure is depicted in Fig. 12. In summary, GNSS data are collected and processed as already described in Section II-D. The 3D-Var module of the WRF model is operated (see Section IV) for each of the SAR overpasses. It produces 3-D fields of temperature, pressure, and water vapor partial pressure used to derive a refractivity 3-D field. The latter is then integrated along a zenith path, using the equation in Section II-A, to obtain the needed ZTD maps from the model, with a DEM providing the lower bound of the integral. The other pipeline processes the SAR data and produces the APS stack to be calibrated using the same GNSS dataset. Once the APSs are converted to zenith delays using the mapping function, the two

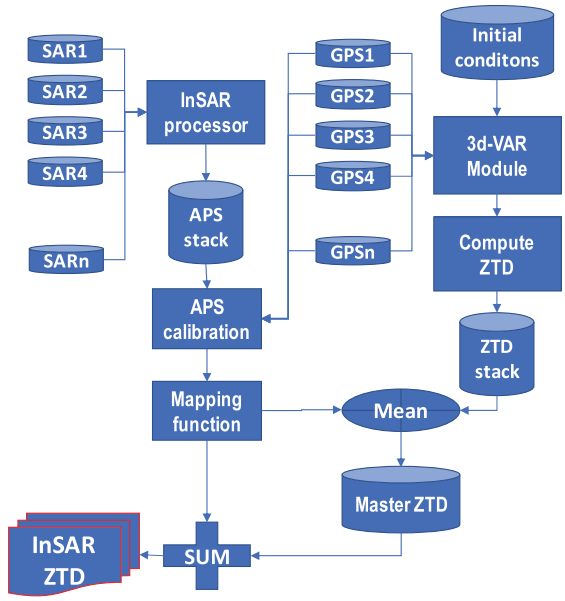

Fig. 12. Data flow of the overall procedure having as input the stack of SAR images and of GNSS estimates and as output the InSAR ZTD maps.

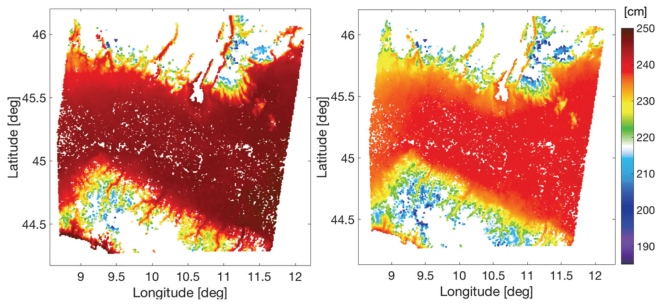

Fig. 13. ZTD maps (in cm) derived from Sentinel-1 (SAR-ZTD) to be assimilated into the NWP model for the two case studies. Left panel: Case study 1 on 27th April 2015. Right panel: Case study 2 on 11th November 2016.

stacks, i.e., ZTDs from the model, and APSs from InSAR are averaged to retrieve the ZTD map of the master which is added to each APS to derive the final product (SAR-ZTD).

We remind here that 3D-Var maps are generated using WRF at resolution of 1 km (see Section IV), whereas more accurate and detailed elevation data are used in GNSS and SAR data processing. So, inevitable inconsistencies can be found between the GNSS-ZTD injected in the assimilation and the resulting ZTD maps produced by the WRF assimilation module. Namely, a couple of GNSS stations presented an anomalous behavior due to a discrepancy of more than 50 m in altitude between the WRF DEM and the actual elevation of the station. Those situations were identified and properly removed.

Examples of the procedure result (in the sequel we refer to the SAR derived absolute ZTD as SAR-ZTD) are shown in Fig. 13 for the two selected case studies.

C. Validation of the Path Delay Maps

Once converted into absolute values, SAR retrieved ZTD generally reproduces the GPS-ZTD at the station positions

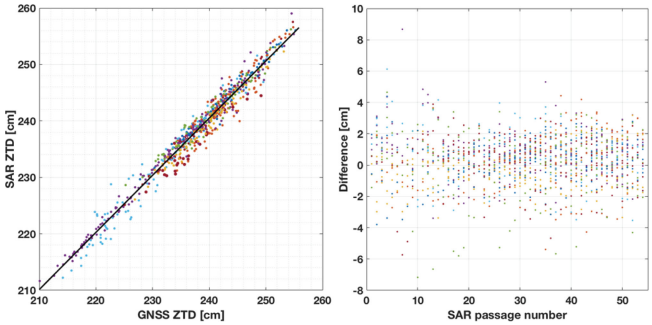

Fig. 14. Comparison between absolute excess path from Sentinel-1 (SAR-ZTD) at the GPS station location and the absolute ZTD from GPS (GNSS-ZTD). Left panel shows the scatterplot of SAR-ZTD versus GPS-ZTD, right panel shows their difference as a function of time (i.e., SAR overpasses count).

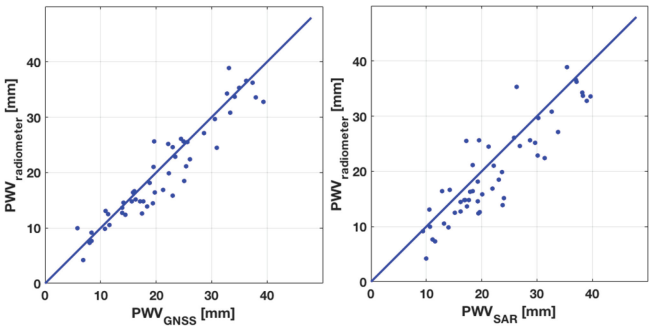

Fig. 15. Comparison between PWV derived from SAR and GNSS with that retrieved by the radiometer at Spino d'Adda location. Left panel: $\mathrm{PWV_{rad}}$ versus $\mathrm{PWV_{GNNS}}$. Right panel: $\mathrm{PWV_{rad}}$ versus $\mathrm{PWV_{SAR}}$.

(apart from DEM errors previously addressed). This is shown in Fig. 14, where the difference standard deviations is at the cm level (1.32 cm).

In order to carry out an independent validation of both GNSS and SAR products, we considered the Spino d'Adda ground-based microwave radiometer measurements (whose position, 30 km east of Milan, 45.4 N e 9.5 E, is shown in Fig. 7). The radiometer is property of the Italian Space Agency (ASI) and operated by Politecnico di Milano in the frame of the Alphasat Aldo Paraboni Scientific Experiment [35]. More details about the instrument and the retrieval algorithm can be found in [36].

From the radiometer, we got a PWV value for each SAR overpass time. Additional ancillary data of surface pressure, temperature, and relative humidity, collected by the meteorological station installed in the same site, were used to convert the ZTDs from GNSS and SAR into corresponding $\mathrm{PWV_{GNSS}}$ and $\mathrm{PWV_{SAR}}$ values for the comparison, as done in [37]. The nearest available GNSS station is, in most of the cases (33 out of 54), at 15 km distance; in some days the comparison was carried out against further stations at 22, 35, 42, and 70 km distance from Spino d'Adda. The scatterplots are reported in Fig. 15. The standard deviation of the differences between radiometer and GNSS PWV's is 2.9 mm, with a bias of 0.5 mm while for the SAR case, the standard deviation is 4.0 mm with a bias of 2.3 mm. Considering the simplified relation in (6) between PWV and zenith delay, those differences correspond, respectively, to 1.9 and 2.4 cm standard deviation for *ZWD*,

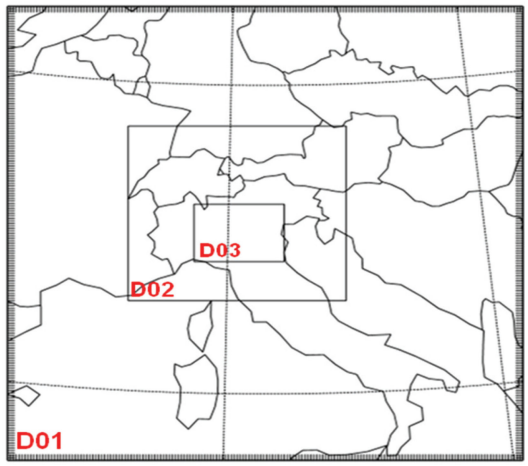

Fig. 16. Three two-way nested domain configurations: D01 = 9 km (176×183 grid points), D02 = 3 km (223×211 grid points), D03 = 1 km (277×208 grid points) with 40 vertical levels.

which is comparable, although a bit larger, to the standard deviation of 1.32 cm between SAR and GNSS-ZTD. One can conclude that GNSS-ZTD slightly outperforms SAR-ZTD in the comparison with the radiometer in that specific site, but the accuracy of the high-resolution and large-coverage SAR-ZTD maps can compete with other instrumentation.

IV. NWP Data Assimilation

A. WRF Model and the Assimilation Technique

The ARW modeling system, version 3.7.1, is used in this work [38]. Three two-way nested domains were used (i.e., D01, D02, D03) centered over the Po Valley area. The model configuration was the following: D01 at 9 km, D02 at 3 km, and D03 at 1 km (see Fig. 16), together with 40 (unevenly spaced) vertical levels. Model simulations were initialized using the analyses of the European Centre for Medium-Range Weather Forecasts (ECMWF) at 0.125° horizontal resolution (about 10 km at the considered latitudes).

To parameterize the subgrid scale processes, we considered Mellor–Yamada–Janjic for the planetary boundary layer, New Thompson for the microphysics, RRTM and Dudhia for the longwave and shortwave radiation, respectively, Eta similarity and Noah land surface model for surface layer and land surface, building environment parameterization as urban surface for all domains, Kain–Fritsch for convection that was activated only on D01. The reader can refer to [38] for details. For the variational (Var) DA technique, refer to [38].

The aim of the 3D-Var approach is to produce the best compromise between an *a priori* estimation of the analysis field and the observations, through the iterative solution that minimizes the *cost function J*. This cost function J measures the distance of a field x from the observations y^0 and from the background x^b. These distances are scaled through the matrices R and B_0, i.e., the observational error covariance matrix and the error covariance matrix of the background, respectively. The cost function for

3D-Var is

$$J(X) = J^B + J^0 = \frac{1}{2}\left\{\left[y^0 - H(x)\right]^T R^{-1}\left[y^0 - H(x)\right] + (x - x^b)^T B_0^{-1}(x - x^b)\right\} \quad (11)$$

where x^b is the generic variable of an *a priori* state (first guess), y^0 is the observation, and H is the operator that converts the model state to the observations space. R also takes into account other errors, such as representativeness and forward operator errors. A detailed description of the 3D-Var system can be found in [39] and [40].

In this work, the data ingested into the assimilation procedure were the ZTD retrieved from GNSS or from SAR. Therefore, the operator H had to convert the model temperature, pressure, and humidity profiles into ZTD by integrating both the dry and wet components of the atmospheric refractivity. Y.-R. Guo implemented such an operator in the DA module of WRF (WRFDA) based on (4) and (5) using a simple trapezoidal formula [24].

A good estimation of the error matrices is important for producing worthwhile initial conditions (IC). R is usually independent of weather conditions and for GNSS- and SAR-ZTD DA, the quality control field that contains the observation error information was set in our cases to be equal to 15 mm. On the other hand, B_0 is weather conditioned and flow dependent, and it depends on the background. Therefore, B_0 must be estimated using a statistical method. The commonly used 3D-Var background error statistics in WRF is based on the NMC-method, which uses a long time series of previous forecasts [41]. In this study, the background error statistics is computed on D03 domain (1 km) for each case study for a period of one week [42].

In the experiments, in order to assess the impact of DA, a preliminary "control" (or "reference") simulation without any DA (hereafter, WRF CTRL) was run from 00:00 UTC to the 00:00 UTC of the following day for both test cases (27th April 2015 and 11th November 2016) using the WRF model. This starting time was chosen with the aim of reproducing the condition of an operational forecast, whose IC and boundary conditions (BC) are generally available at 00:00 or 12:00 UTC. As for the assimilation experiment, SAR-ZTD was available around six hours after the ECMWF initialization data and therefore, the approach depicted in Fig. 17 was adopted. Namely, a *warm start* (or *cycling mode*) simulation (green bar in Fig. 17) was initiated at 00:00 UTC to provide the background fields at 06:00 UTC. This time was selected as the "*analysis time*" of the procedure (blue star in Fig. 17) when the ZTD observations from GNSS or SAR were assimilated, producing the forecasted fields denoted as WRF GNSS or WRF SAR, respectively. This start time was close, but not exactly equal, to the SAR acquisition time (@05:24:30 for 27th April 2015 and @05:19:09 for 11th November 2016), so that the hypothesis of a frozen atmosphere (i.e., no change of the atmosphere conditions) was assumed between the SAR acquisition and the analysis time, which is justified by the persistent meteorological condition during this time. The warm start procedure should ensure a sufficient *spin-up time* (the initial spin-up period required in order for the mesoscale model to adjust its high-resolution domains to the given conditions), which is in the order of 6 h.

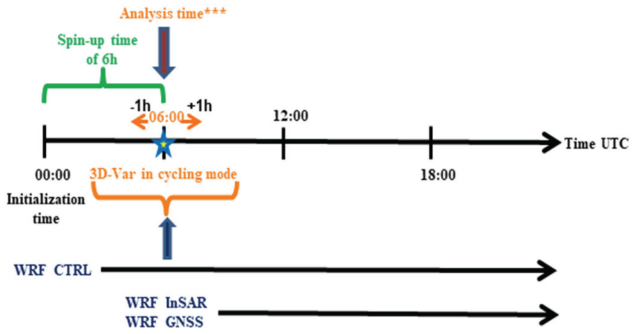

Fig. 17. Scheme of the assimilation procedure: The assimilation time (06:00 UTC) corresponds to the SAR acquisition time (more or less) and the output of a previous WRF forecast is chosen as first guess.

The selected time window for the assimilation was 1 h, which means that all the GNSS observations in the interval of ± 1 h around the *analysis time* were processed. For example, the observations between 05:00 and 07:00 UTC were treated as the observations at 06:00 UTC. As for the SAR-ZTD, this is not applicable.

With the aim of producing more accurate analyses, the *outer loop* procedure was adopted for both WRF GNSS and WRF SAR [43]. It aims at excluding low-quality observations, but it also takes into account the nonlinearities in the observation operator and the small-scale features of the observed fields. The outer loop procedure includes observations that were rejected by the previous loop, but pass the background quality control checks, so that they are accepted in the subsequent outer loop, and thus, finally influence the analysis. For both simulations, three outer loops were chosen. For example, as for case study 1, a total of 24 665 SAR observations were ingested in the first outer loop, 24 686 in the second, and 24 683 in the third one. For case study 2, a total of 24 680 SAR observations were assimilated in the innermost outer loop, 24 692 in the second, and 24 690 in the third one. After the assimilation, the lateral and lower BCs were updated for the high-resolution forecast at 1 km. Finally, the new IC and BC were used for the model initialization at 06:00 UTC. It must be pointed out that although a site dependent bias correction is generally applied for operational usage of GNSS_ZTD in NWP, based on the GNSS_NWP ZTD offsets, no bias correction with respect to the model background was performed in this study.

Before running WRF, a preliminary analysis was performed to verify the information brought by the novel SAR product with respect to the common approach relying on a GNSS network. In particular, we compared the SAR-ZTD maps generated by the procedure depicted in Section III-B to the output of the 3D-Var assimilating the GNSS-ZTD only. This comparison is shown in Fig. 18 for the two selected events, on the knots of the 3D-Var grid. According to the color bar, bluish colors indicate higher values of ZTD introduced by SAR, while greenish and reddish color the opposite, as will be discussed in the next section. The estimated error matrix B_0 enables very localized difference in the maps.

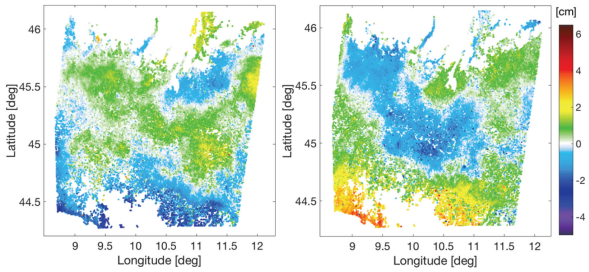

Fig. 18. Difference, in cm, between ZTD produced by 3D-Var after assimilation of GNSS-ZTDs and the SAR-ZTD map for April 27th 2015 (left) and November 11th 2016 (right).

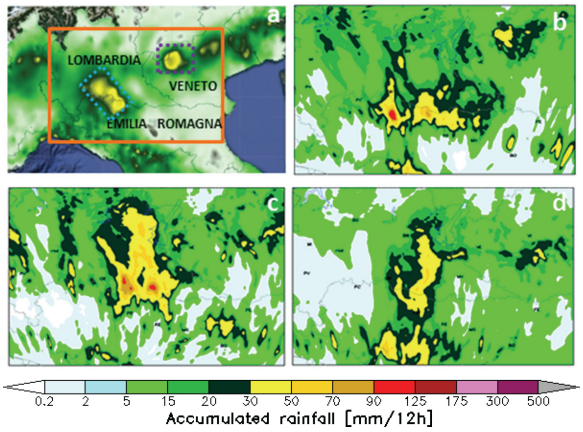

Fig. 19. Twelve-hour accumulated rainfall until 00:00 UTC of Tuesday, 28th April 2015 from: (a) DEWETRA rain gauges; (b) WRF output without assimilation (WRF CTRL); (c) WRF output assimilating GPS-ZTD using three outer loops (WRF GNSS); and (d) WRF output assimilating SAR-ZTD using three outer loops (WRF SAR).

B. Case Study 1 Assimilation Results

At first, the results of the model forecasts with and without assimilation are compared to the rain rate maps derived from the rain gauge network of the DEWETRA platform. In Fig. 18(a), the 12-h accumulated rainfall until 00:00 UTC on Tuesday, 28th April 2015 is chosen for the comparison. The orange box in the upper left panel of Fig. 19(a) reproduces the D03 domain; we focus the attention on the two rainfall cells in the colored dashed squares—a general overestimation of the extension of the area interested by the precipitation is found in all the model simulations. Above all, WRF CTRL and WRF GNSS show some convective cells with accumulated precipitation between 90 and 125 mm/12 h [see reddish spots in Fig. 19(b) and (c)] that are clearly overestimated with respect to Fig. 19(a). These two simulations overestimate the precipitation also over the Po Valley by producing several isolated cells of 30–50 mm/12 h that are not observed. On the other hand, WRF CTRL is capable of reproducing the cell in the violet dashed square of Fig. 19(a) over the Veneto region.

On the contrary, the assimilation of SAR data [WRF SAR, Fig. 19(d)] shows a positive impact in the Po Valley, by reducing the amount of rainfall represented by the reddish spots and making the isolated cells that were not observed by the rain gauges disappear. Furthermore, the cell over the Veneto region is reduced and shifted toward southeast by WRF SAR.

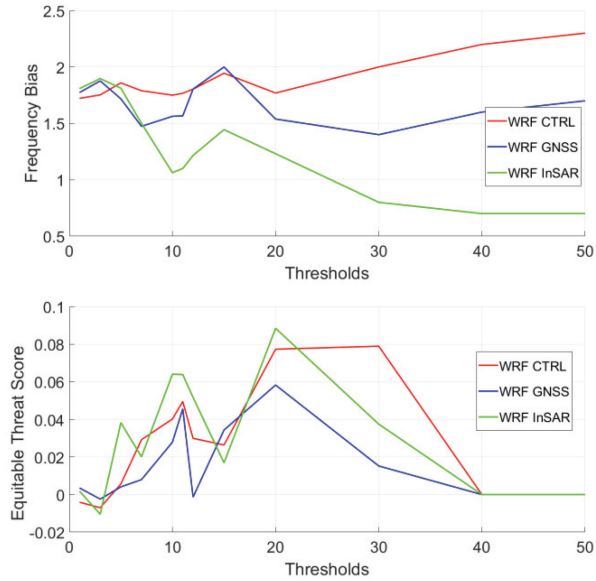

Fig. 20. FBIAS (upper panel) and ETS (bottom panel) referred to each experiment (WRF CTRL red curve, WRF GNSS blue curve, and WRF SAR green curve) for the case study 1 and for threshold values of 5, 10, 15, 20, 25, 30, 35, 40, 45, and 50 mm/12 h.

A quantitative assessment was also carried out considering the rain gauges data coming from the DEWETRA platform and the trend of 12 h accumulated precipitation from WRF simulations. Two statistical indices, i.e., the frequency bias (FBIAS) and the equitable threat score (ETS) (see [44]) were calculated for each experiment on the D03 domain considering threshold values for the cumulated rain rate from 5 to 50 mm/12 h.

FBIAS is the ratio between the number of forecasted rainy cells (i.e., cells with rain rate above the threshold) and that of the observed ones, and goes from zero to infinity. ETS is the ratio between the number of hits in the detection of rainy cells (corrected to account for hits due to chance) and the sum of number of hits, missed detections, and false alarms and goes from $-1/3$ to 1. The best value for both indexes is 1, which corresponds to a perfect forecast. A total of 487 rain gauges were available in the inner domain for case study 1.

The comparison was performed using the *point_stat* tool that is a module of the model evaluation tools (MET) embedded in the WRF package. In most cases, there is not an exact match between the grid nodes and the pluviometer positions; therefore, a 2×2 grid size is defined around each observation point. The expected accumulated precipitation is determined by averaging the values of the four nodes closest to the considered rain gauge. The two statistical indexes are shown in Fig. 20 as a function of the above-mentioned threshold values. For the FBIAS index, WRF CTRL and WRF GNSS (red and blue curve, respectively) produce the worst values for all thresholds, whereas WRF SAR (green curve) shows an overall better performance. High values of FBIAS (around 1.8–1.9) are found for low precipitation threshold (until 5 mm/12 h) for all the experiments, whereas values closer to 1 are found for WRF SAR and the greater threshold

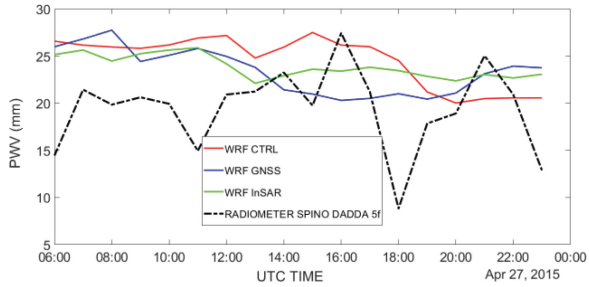

Fig. 21. Comparison between PWV (in mm) measured by the Spino d'Adda radiometer and predicted by WRF model for case study 1, as a function of time starting from the assimilation time at 06:00 UTC. WRF CTRL, WRF GNSS, and WRF SAR are the red, blue, and green curves, respectively, whereas the Spino d'Adda radiometer is the black dash-dot curve.

values. Especially, between 30 and 50 mm/12 h, FBIAS stays around 0.6/0.8. Concerning the ETS, even though values are generally poor, WRF SAR exhibits quite competitive values up to a threshold value of 20 mm/12 h, while degrading for higher thresholds, but staying higher with respect to WRF GNSS until a threshold of 40 mm/12 h.

These indices confirm that the main improvement brought by SAR-ZTD assimilation is the mitigation of the high rain cells overvalued by the other experiments. Going back to Fig. 18, this effect could be associated with the lower values of SAR-ZTD injected into the 3D-Var module in the eastern side of the area corresponding to the Po Valley (negative values color coded in green) compared to the map of ZTD produced by the GNSS DA.

An additional assessment of the forecasts was performed using the data of PWV coming from the radiometer located in Spino d'Adda (see Section III-C). The comparison is shown as a function of time in Fig. 21. It is understood that this comparison covers a single point in the whole model domain.

At the start time (06:00 UTC), values of approximately 10–12 mm, larger than the radiometer retrievals (black dashed line), are produced by all the model runs until 11:00 UTC. After this time, the PWV's produced by WRF GNSS and WRF SAR tend to get closer to the one of the radiometers, even though missing the sharp variation between 16:00 and 21:00 UTC. In general, all the PWV model estimates show a quite similar trend in time, but WRF CTRL produces the largest overestimation, except for the last 6-h of the simulation.

C. Case Study 2 Assimilation Results

Similarly to case study 1, an analysis of the 12-h accumulated rainfall until 00:00 UTC of Saturday, 12th November 2016 was performed. In Fig. 22 (panel on the top left), the interpolated rainfall observed by the DEWETRA rain gauges network is compared to the WRF outcomes. According to the rain gauges [see the orange box of Fig. 22(a)], there is no rainfall in Lombardy region and in the west part of Emilia Romagna; most of the rainfall is in Veneto and in the eastern part of Emilia Romagna. The 12-h accumulated rainfall from the WRF simulations [see Fig. 22(b)–(d)] shows large differences among them. This suggests a sensible impact of the assimilation of both GNSS- and SAR-derived products. A large underestimation by

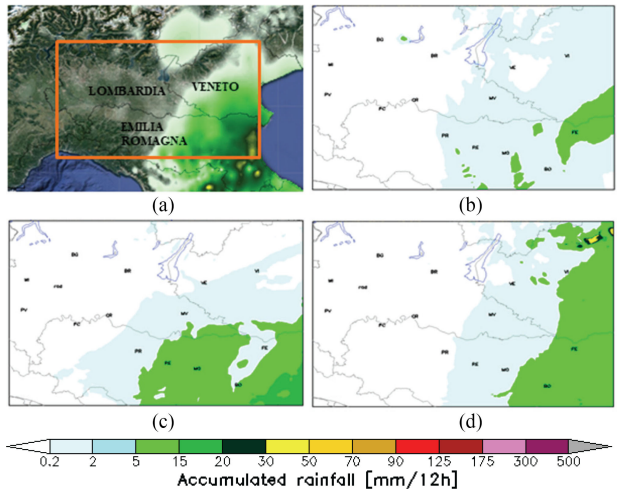

Fig. 22. As in Fig. 19, but for 12-h accumulated rainfall until 00:00 UTC of Saturday, 12th November 2016.

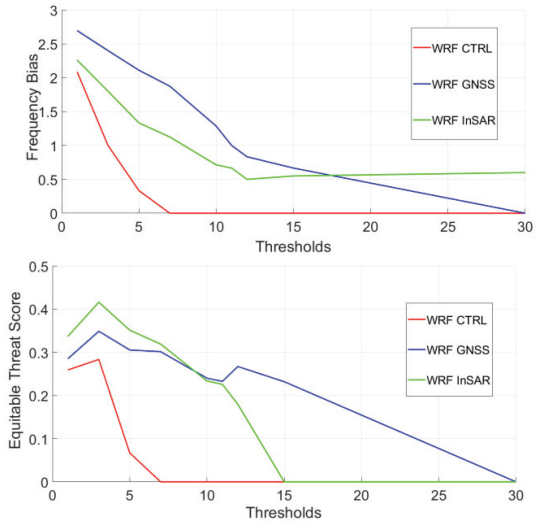

Fig. 23. As in Fig. 20, but for case study 2 and for threshold values of 5, 10, 15, 20, 25, 30 mm/12 h.

WRF CTRL [see Fig. 22(b)] is found, which is mitigated by the assimilation of GNSS-ZTD and SAR-ZTD. An underestimation of the rainfall still persists for WRF GNSS [see Fig. 22(c)], whereas a good agreement between the model and the observation is found for the WRF SAR [see Fig. 22(d)] for what concerns both the location of the precipitation pattern and its intensity. In this case, the green pattern is well reproduced also in Veneto region, but an overestimation is found in the northeast of the domain (small yellow cells in the upper right corner). Overall, this qualitative assessment suggests a positive impact of the SAR DA.

Concerning the statistical assessment, similarly to case study 1, FBIAS and ETS are shown in Fig. 23, but the maximum threshold values are limited to 30 mm/12 h because this event is much drier than the other one. A total of 465 rain gauges are available for case study 2.

In Fig. 23, the FBIAS index shows a quite similar decreasing trend for all the three simulations for threshold values up to

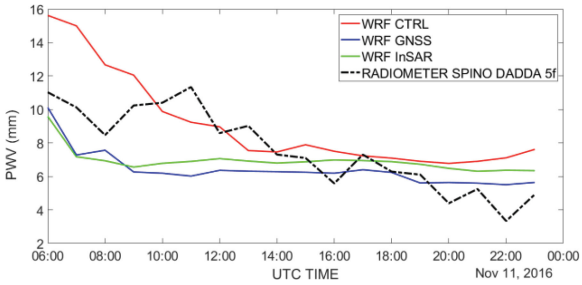

Fig. 24. As in Fig. 21, but for case study 2.

6–7 mm/12 h, even though all the curves start from a very high value of the index. WRF CTRL (red curve) degrades towards zero very quickly, similarly to what WRF GNSS (blue curve) does, but more gradually. Vice versa, WRF SAR (green curve) is the only one that keeps fairly good values (with FBIAS in a range of 0.5–1) for threshold values from 15 to 30 mm/12 h. For what concerns the ETS index, WRF SAR (green curve) clearly shows the best values until a threshold of approximately 10 mm/12 h, whereas WRF GNSS (blue curve) is able to produce high values even for higher thresholds. WRF CTRL is the one that returns the worst result. In summary, this case is characterized by a quite small precipitation rate and the WRF runs are not substantially different. Nonetheless, the assimilation of SAR-ZTD helps produce reasonably high rain rate values (above 15 mm/12 h), where the other experiments fail. Also, in this case, there is a confirmation in the right map of Fig. 18, where the bluish area in the central part indicates that SAR-ZTD is injecting higher path delay in the assimilation as compared to the reference ZTD field determined by GNSS assimilation only.

As in the previous section, the PWV from the radiometer of Spino d'Adda is also considered for a pointwise comparison with WRF results as function of time. In Fig. 24, the comparison between PWV from the radiometer and the WRF simulations clearly shows an overestimation of the WRF CTRL (red curve) of about 5 mm and a small underestimation in the PWV (1–1.2 mm) for both WRF GNSS and WRF InSAR (blue and green curves, respectively) at the start time. On the other hand, WRF CTRL from 10:00 UTC becomes closer to the temporal profile of the radiometer. In the same way, WRF GNSS and WRF SAR, which have a behavior almost parallel from 09:00 to 23:00 UTC, tend to get closer to the black dashed line that represents the Spino d'Adda radiometer PWV estimation.

The time series show the positive impact at the start time for both events but rapidly converging toward the WRF CTRL simulation. The loss of impact after a few hours from the start time is a known result for any type of data in the assimilation procedure. The different results obtained for the two events arise from the quite diverse synoptic situation of the two events—the first one can be classified as a "moderate/heavy precipitation event," the second one as a "light rainfall event."

V. Conclusion

An overall approach to derive absolute ZTD from InSAR was developed. Novel methodologies were proposed for what concerns the combination of GNSS receiver data and APS from InSAR for calibration purposes (removal of the unknown bias as well orbital error effects in the interferograms). The capability of InSAR to sense the horizontally variable stratification of the atmosphere, leading to different vertical trends of APSs as function of surface height, was discussed. More importantly, a method to retrieve the absolute path delay from the differential APS was proposed, rooted in the concept of multipass InSAR data processing and on the assumption of an operational exploitation of a numerical weather forecast model in the considered geographical area. It is based on the estimation of a "mean" atmosphere from the model itself, and it reduces the errors associated to other methods, such as trusting the knowledge of the atmosphere at a certain time. This approach may be particularly suited for APSs derived from a geosynchronous SAR observing the earth at continental scale with short revisit time.

The product of this method is a map of total tropospheric path delay at the spatial resolution of the InSAR interferometric stack (order of hundreds of meters). It was validated against the GNSS retrievals (about 1.32 cm difference standard deviation) and a pointwise independent information derived from a microwave radiometer (about 2.4 cm difference standard deviation).

The ZTD map derived from InSAR (instead of the PWV, as proposed in other works) was then assimilated within the WRF weather prediction numerical model. The justification of this choice is twofold—InSAR is directly measuring the total delay, so the derivation of PWV requires to relay on the model itself to remove the dry component; moreover, the information brought by SAR on the vertical stratification of the atmosphere is fully exploited.

The improvement in the prediction skill by assimilating InSAR derived ZTD was assessed for two case studies. A qualitative and quantitative comparison of the forecasts with the data from a rain gauge network and with the columnar water vapor provided by a microwave radiometer showed a moderate but nevertheless evident positive impact of the InSAR product. Its assimilation mitigated the overprediction of rain rate cells in one case, and the underestimation of rain rate in the other case.

The overall proposed methodology is rooted in past works, but it also introduces novel solutions. In particular, the derivation of the absolute columnar values via the two pipelines of SAR and NWP processing is time consuming, but at the same time, easy to implement in an operational environment. For a better exploitation of a geosynchronous SAR, the 4D-Var assimilation and a slant total delay observation operator should be considered in the future.

Acknowledgment

The authors would like to thank S. Zoffoli from ASI for her support and fruitful discussions. The authors would also like to thank ASI for supporting the Alphasat Aldo Paraboni propagation experiment, and L. Luini and C. Riva for providing the processed radiometric data. The authors would also like to acknowledge the LNGS and NCAR Laboratories, as well as DPC and CIMA Research Foundation.

REFERENCES

[1] E. Pichelli, R. Rotunno, and R. Ferretti, "Effects of the Alps and Apennines on forecasts for Po Valley convection in two HyMeX cases," *Quart. J. Roy. Meteorol. Soc.*, vol. 143, pp. 2420–2435, Aug. 2017, doi: 10.1002/qj.3096.

[2] C.-H. Moeng, J. Dudhia, J. Klemp, and P. Sullivan, "Examining two-way grid nesting for large eddy simulation of the PBL using the WF model," *Monthly Weather Rev.*, vol. 135, pp. 2295–2311, 2007.

[3] R. F. Hanssen, T. M. Weckwerth, H. A. Zebker, and R. Klees, "High-resolution water vapor mapping from interferometric radar measurements," *Science*, vol. 283, no. 5406, pp. 1297–1299, 1999.

[4] R. F. Hanssen, *Radar Interferometry: Data Interpretation and Error Analysis*. Dordrecht, The Netherlands: Springer, 2001.

[5] A. Ferretti, C. Prati, and F. Rocca, "Permanent scatterers in SAR interferometry," *IEEE Trans. Geosci. Remote Sens.*, vol. 39, no. 1, pp. 8–20, Jan. 2001.

[6] P. Berardino, G. Fornaro, R. Lanari, and E. Sansosti, "A new algorithm for surface deformation monitoring based on small baseline differential SAR interferograms," *IEEE Trans. Geosci. Remote Sens.*, vol. 40, no. 11, pp. 2375–2383, Nov. 2002.

[7] S. Hobbs, C. Mitchell, B. Forte, R. Holley, B. Snapir, and P. Whittaker, "System design for geosynchronous synthetic aperture radar missions," *IEEE Trans. Geosci. Remote Sens.*, vol. 52, no. 12, pp. 7750–7763, Dec. 2014.

[8] E. Pichelli *et al.*, "Water vapour distribution at urban scale using high-resolution numerical weather model and spaceborne SAR interferometric data," *Natural Hazards Earth Syst. Sci.*, vol. 10, pp. 121–132, 2010.

[9] P. Mateus, G. Nico, R. Tomé, J. Catalão, and P. M. A. Miranda, "Experimental study on the atmospheric delay based on GPS, SAR interferometry, and numerical weather model data," *IEEE Trans. Geosci. Remote Sens.*, vol. 51, no. 1, pp. 6–11, Jan. 2013.

[10] E. Pichelli *et al.*, "InSAR water vapor data assimilation into mesoscale model MM5: Technique and pilot study," *IEEE J. Select. Topics Appl. Earth Observ. Remote Sens.*, vol. 8, no. 8, pp. 3859–3875, Aug. 2015.

[11] F. Alshawaf, S. Hinz, N. Mayer, and J. F. Meyer, "Constructing accurate maps of atmospheric water vapor by combining interferometric synthetic aperture radar and GNSS observations," *J. Geophys. Res. Atmos.*, vol. 120, pp. 1391–1409, 2015, doi: 10.1002/2014JD022419.

[12] L. Chang,, M. Liu, L. Guo, X. He, and G. Gao, "Remote sensing of atmospheric water vapor from synthetic aperture radar interferometry: Case studies in Shanghai, China," *J. Appl. Remote Sens.*, vol. 10, no. 4, 2016, Art. no. 046032.

[13] W. Tang,, M. Liao, L. Zhang, W. Li, and W. Yu, "High-spatial-resolution mapping of precipitable water vapor using SAR interferograms, GPS observations and ERA-Interim reanalysis," *Atmos. Meas. Techn.*, vol. 9, no. 9, pp. 4487–4501, 2016.

[14] P. Mateus, R. Tomé, G. Nico, and J. Catalão, "Three-dimensional variational assimilation of InSAR PWV using the WRFDA model," *IEEE Trans. Geosci. Remote Sens.*,vol. 54, no. 12, pp. 7323–7330, Dec. 2016.

[15] P. Mateus, J. Catalão, and G. Nico, "Sentinel-1 interferometric SAR mapping of precipitable water vapor over a country-spanning area," *IEEE Trans. Geosci. Remote Sens.*, vol. 55, no. 5, pp. 2993–2999, May 2017.

[16] P. Mateus, J. Catalão, G. Nico, and P. Benevides, "Mapping precipitable water vapor time series from Sentinel-1 interferometric SAR," *IEEE Trans. Geosci. Remote Sens.*, vol. 58, no. 2, pp. 1373–1379, Feb. 2020.

[17] M. Lagasio *et al.*, "A synergistic use of a high-resolution numerical weather prediction model and high-resolution earth observation products to improve precipitation forecast," *Remote Sens*., vol. 11, 2019, Art. no. 2387.

[18] P. M. A. Miranda *et al.*, "InSAR meteorology: High- resolution geodetic data can increase atmospheric predictability," *Geophys. Res. Lett.*, vol. 46, pp. 2949–2954, Feb. 2019, doi: 10.1029/2018GL081336.

[19] G. Mulder, F. van Leijen, J. Barkmeijer, S. de Haan, and R. Hanssen, "Towards assimilation of InSAR data in operational weather models," *Geophys. Res. Abstr.*, vol. 19, 2017, Art. no. 14387.

[20] E. Sansosti, F. Casu, M. Manzo, and R. Lanari, "Space-borne radar interferometry techniques for the generation of deformation time series: An advanced tool for Earth's surface displacement analysis," *Geophys. Res. Lett.*, vol. 37, Oct. 2010, Art. no. L20305, doi: 10.1029/2010GL044379.

[21] G. Fornaro, G. Franceschetti, R. Lanari, E. Sansosti, and M. Tesauro, "Global and local phase unwrapping techniques: A comparison," *J. Opt. Soc. Amer. A*, vol. 14, no. 10, pp. 2702–2708, Oct. 1997.

[22] G. Fornaro and E. Sansosti, "A two-dimensional region growing least-squares phase unwrapping algorithm for interferometric SAR processing," *IEEE Trans. Geosci. Remote Sens.*, vol. 37, no. 5, pp. 2215–2226, Sep. 1999.

[23] F. Meyer, R. Bamler, N. Jakowski, and T. Fritz, "The potential of low frequency SAR systems for mapping ionospheric TEC distributions," *IEEE Geosci. Remote Sens. Lett.*, vol. 3, no. 4, pp. 560–564, Oct. 2006.

[24] E. Vedel and X. Y. Huang, "Impact of ground based GPS data on numerical weather prediction," *J. Meteorol. Soc. Japan*, vol. 82, pp. 459–472, 2004.

[25] M. Bevis *et al.*, "GPS meteorology: Remote Sensing of atmospheric water vapor using the global positioning system," *J. Geophys. Res.*, vol. 97, pp. 15787–15801, 1992.

[26] F. Pignone *et al.*, "GRISO (Random Generator of Space interpolations from uncertain observations)-Rain," (in Italian), Activity report of the first year concerning the Agreement 778/2009 between the Department of Italian Civil Protection and CIMA Foundation, Rep. 272/2010, p. 353, 2010.

[27] C. de Luca *et al.*, "An on-demand web tool for the unsupervised retrieval of earth's surface deformation from SAR data: The P-SBAS service within the ESA G-POD environment," *Remote Sens.*, vol. 7, pp. 15630–15650, 2015.

[28] C. de Luca, I. Zinno, M. Manunta, R. Lanari, and F. Casu, "Large areas surface deformation analysis through a cloud computing P-SBAS approach for massive processing of DInSAR time of DInSAR time series," *Remote Sens. Environ.*, vol. 202, pp. 3–17, 2017.

[29] A. Pepe, P. Berardino, M. Bonano, L. D. Euillades, R. Lanari, and E. Sansosti, "SBAS-based satellite orbit correction for the generation of DInSAR time-series: Application to RADARSAT-1 data," *IEEE Trans. Geosci. Remote Sens.*, vol. 49, no. 12, pp. 5150–5165, Dec. 2011.

[30] E. Realini and M. Reguzzoni, "goGPS: Open source software for enhancing the accuracy of low-cost receivers by single-frequency relative kinematic positioning," *Meas. Sci. Technol.*, vol. 24, Oct. 2013, Art. no. 115010.

[31] A. M. Herrera, H. F. Suhandri, E. Realini, M. Reguzzoni, and M. C. de Lacy, "goGPS: Open-source MATLAB software", *GPS Solutions*, vol. 20, no. 3, pp. 595–603, 2016.

[32] J. Kouba and P. Héroux, "Precise point positioning using IGS orbit and clock products," *GPS Solutions*, vol. 5, no. 2, pp. 12–28, 2001.

[33] S. Barindelli, E. Realini, G. Venuti, A. Fermi, and A. Gatti, "Detection of water vapor time variations associated with heavy rain in northern Italy by geodetic and low-cost GNSS receivers," *Earth, Planets Space*, vol. 70, 2018, Art. no. 28, doi: 10.1186/s40623-018-0795-7.

[34] F. Onn, "Modeling water vapor using GPS with application to mitigating InSAR atmospheric distortions," Ph.D. dissertation, Stanford University, Stanford, CA, USA, Nov. 2006.

[35] T. Rossi *et al.*, "Satellite communication and propagation experiments through the Alphasat Q/V band Aldo Paraboni technology demonstration payload," *IEEE Aerosp. Electron. Syst. Mag.*, vol. 31, no. 3, pp. 18–27, Mar. 2016.

[36] L. Luini and C. Capsoni, "Using NWP reanalysis data for radiometric calibration in electromagnetic wave propagation experiments," *IEEE Trans. Antennas Propag.*, vol. 64, no. 2, pp. 70–707, Feb. 2016.

[37] H. Vedel, K. S Mogensen, and X. Y. Huang, "Calculation of zenith delays from meteorological data comparison of NWP model, radiosonde and GPS delays," *Phys. Chem. Earth A, Solid Earth Geodesy*, vol. 26, no. 6/8, pp. 497–502, 2001.

[38] W. C. Skamarock *et al.*, "A description of the Advanced Research WRF version 3," Nat. Center Atmos. Res., Boulder, CO, USA, NCAR Tech. Note NCAR/TN-475+STR, 2008.

[39] D. M. Barker, W. Huang, Y. G. Guo, and A. Bourgeois, "A three-dimensional variational (3DVAR) data assimilation system for use with MM5," Nat. Center Atmos. Res., Boulder, CO, USA, NCAR Tech. Note NCAR/TN-453+STR, 2003.

[40] D. M. Barker, W. Huang, Y. R. Guo, A. Bourgeois, and Q. Xiao, "A three-dimensional variational (3DVAR) data assimilation system for use with MM5: Implementation and initial results," *Monthly Weather Rev.*, vol. 132, pp. 897–914, 2004.

[41] D. F. Parrish and J. C. Derber, "The National Meteorological Center's spectral statistical-interpolation analysis system," *Monthly Weather Rev.*, vol. 120, pp. 1747–1763, 1992.

[42] S. Sugimoto, N. A. Crook, J. Sun, Q. Xiao, and D. M. Barker, "An examination of WRF 3DVAR radar data assimilation on its capability in retrieving unobserved variables and forecasting precipitation through observing system simulation experiments," *Monthly Weather Rev.*, vol. 137, pp. 4011–4029, 2009.

[43] L.-F. Hsiao *et al.*, "Application of WRF 3-DVAR to operational typhoon prediction in Taiwan: Impact of outer loop and partial cycling approaches," *Weather Forecast*, vol. 27, no. 5, pp. 1249–1263, 2012, doi: 10.1175/waf-d-11-00131.1.

[44] D. S. Wilks, *Statistical Methods in the Atmospheric Sciences*, 2nd ed. San Diego, CA, USA: Academic, 2006, p. 627.

Nazzareno Pierdicca (Senior Member, IEEE) received the Laurea (Doctor's) degree in electronic engineering (*cum laude*) from the University "La Sapienza" of Rome, Rome, Italy, in 1981.

From 1978 to 1982, he was with the Italian Agency for Alternative Energy (ENEA), Rome, Italy. From 1982 to 1990, he was with the Remote Sensing Division, Telespazio, Rome, Italy. In November 1990, he joined the Department of Information Engineering, Electronics and Telecommunications, Sapienza University of Rome, Rome, Italy. He is currently a Full Professor and teaches remote sensing, antenna, and electromagnetic fields at the Faculty of Engineering. His research interests include electromagnetic scattering and emission models for sea and bare soil surfaces and their inversion, microwave radiometry of the atmosphere, SAR, bistatic radar, and GNSS-R land applications.

Prof. Pierdicca is a Former Chairman of the IEEE Geoscience and Remote Sensing Society Central Italy Chapter.

Ida Maiello received the Laurea (Doctor's) degree in sciences and technologies of navigation systems (*cum laude*) from the University "Parthenope" of Naples, Naples, Italy, in 2009, and the Ph.D. degree in methods and technologies for environmental monitoring from the School of Engineering, University of Basilicata, Potenza, Italy, in 2013.

From 2010 to 2013, she won a scholarship with the Center of Excellence for Prediction of Severe Events (CETEMPS), University of L'Aquila, L'Aquila, Italy, and within this, she was a Visiting Ph.D. Student with the NCAR Laboratories, Boulder, CO, USA. From 2013 to 2017, she was a Research Fellow with CETEMPS and in addition, from October 2013 to June 2016, she was a Professor of Meteorology with the "G. D'Annunzio" High School, Corropoli, Italy. From 2017 to 2018, she was a Research Fellow with "Sapienza" University of Rome, Rome, Italy. From September 2018 to August 2019, she had her last year with CETEMPS with a scholarship. She is currently a Meteorologist for the Civil Protection of Abruzzo Region, Centro Funzionale d'Abruzzo, L'Aquila, Italy. Her research interests included data assimilation and meteorological modeling, with particular attention to 3D-Var assimilation of radar data, and also, predicting severe weather events.

Eugenio Sansosti (Senior Member, IEEE) received the Laurea degree (*summa cum laude*) in electronic engineering from the University of Napoli "Federico II," Naples, Italy, in 1995.

Since 1997, he has been with the (Italian) National Research Council, Rome, Italy, where he is currently a Researcher Director with the Institute for Electromagnetic Sensing of the Environment (IREA), Naples. He was also an Adjunct Professor of Signal Theory with the University of Reggio Calabria, Italy, in 1999, and of Communication and Signal Theory with the University of Cassino, Cassino, Italy, from 2000 to 2003. He was a Visiting Scientist with the German Aerospace Research Establishment (DLR), Germany, in 1996 and 1997, with the Jet Propulsion Laboratory (JPL), USA, in 1997–1998 and 2000, and with the Istituto Tecnòlogico de Aeronàutica (ITA), Brazil, in 2000. His main research interests include SAR signal processing, with particular emphasis on SAR interferometry and its application to geophysical processes.

Dr. Sansosti was the General Chairman of the First and the Second International Workshops on the Use of Remote Sensing Techniques for Monitoring Volcanoes and Seismogenic Areas (USEReST), in 2005 and 2008, respectively. He also chaired several sessions on international conferences and was a Member of the Editorial Board of the journal *Geomatics*, *Natural Hazards and Risk* edited by Taylor and Francis and is Member of the Editorial Board of *Remote Sensing* edited by MDPI.

Giovanna Venuti was born in 1969. She received the master's degree with honours in civil engineering from Politecnico di Torino, Torino, Italy, in 1993, and the Ph.D. degree in geodesy and surveying from the Politecnico di Milano, Milano, Italy, in 1998, with a thesis on the determination of the mediterranean sea dynamic height from radar altimetry.

Since 1998, she has been a Researcher for the Italian Research Council. She began her academic career with Politecnico di Milano, in 2001. She is currently an Associate Professor, teaching Geospatial data analysis and earth observation for geoinformatics engineering and geostatistics for civil engineering for risk mitigation. Since 2009 she has been involved in national and international projects on GNSS and SAR meteorology. Her research interests include geostatistics and applied geodesy.

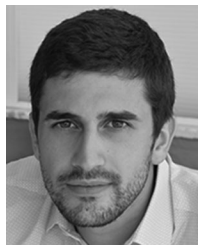

Stefano Barindelli was born in 1992. He received the M.Sc. degree in environmental engineering in 2017 from the Politecnico di Milano, Milano, Italy, where he is currently working toward the Ph.D. degree in geomatics with the Department of Civil and Environmental Engineering.

He is involved in research projects on GNSS and SAR meteorology. His research interests include applications related to GNSS meteorology and nowcasting of severe weather events.

Rossella Ferretti received the Ph.D. degree in geophysics from the School of Geophysical Sciences, Georgia Institute of Technology, Atlanta GA, USA, in 1986, and the second Ph.D. degree in physics and "Laurea" in physics, "*summa cum laude*," from the University of Rome "La Sapienza," Rome, Italy, in 1987.

She is the Director of the master's degree in Atmospheric Science and Technology, University of L'Aquila-University of Rome "Sapienza." From September 2015 to February 2017, she was a Lead Scientist with the Danish Meteorological Institute for Nowcasting and NWP, Copenhagen, Denmark. During 2013–2015, she was the Vice-Coordinator/Director of the Virtual Operational Italian Meteorological Center (VOC), L'Aquila, Italy, during the HyMex campaign (September–November 2012). Since 2006, she has been an Associate Professor with the Department of Physics, University of L'Aquila, L'Aquila, Italy. During 1998–2015, she has taught at least three graduate and undergraduate classes every academic year, among them: Dynamic meteorology, climatology, mesoscale modeling, and laboratory for computational physics. During 2017–2018, she has taught: Dynamic meteorology, physics of fluid, introduction to computational physics. During 2016 – 2018, she taught 3.5 hours the following class "Errors source in NWP" for the Master di II livello in "Analisi e Mitigazione del Rischio Idrogeologico" – Dipartimento di Scienze della Terra. During 2001–2018, she led the Meteorological Modelling Group, Center of Excellence for Prediction of Severe Events (CETEMPS), University of L'Aquila, and in charge of the operational weather forecast at CETEMPS (http://cetemps.aquila.infn.it). She is the author of more than 50 papers in international peer refereed journals. She is an expert in mesoscale modeling. She developed a deep knowledge of the mesoscale modeling MM5 and of the new generation weather research and forecasting model (WRF) from NCAR and is the in charge of several national and international projects.

Dr. Ferretti is the Referee for several international journals, Guest Editor for the *Quarterly Journal of the Royal Meteorological Society* for the special issue "Hymex campaign," Reviewer for the Research Council of Norway for a proposal on orographic precipitation, and for the Netherlands e-Science Center (NLeSC), the Netherlands Organisation for Scientific Research (NWO), and the Italian Super Computing Resource Allocation promoted by CINECA.

Andrea Gatti received the M.Sc. degree in computer engineering and the Ph.D. degree in environmental and infrastructure engineering from the Politecnico di Milano, Milano, Italy, in 2009 and 2014, respectively.

He largely contributed to the development of the spacewise approach for the analysis of gravity data of the ESA-GOCE satellite mission, using which, he computed the global gravity model GO_CONS_GCF_2_SPW_R5, available at the International Centre for Global Earth Models archive. His research is focused on the development of code for data analysis with a special attention to processing performances and parallel execution. At the beginning of 2017, he oriented his studies to the analysis of GNSS data and started working on a project aiming to tropospheric analysis through the usage of GNSS data for the calibration of SAR APS data. He became one of the major contributors to the open-source software called goGPS, an application for the analysis of GNSS data. In 2017, he started a new development branch that led to large improvements in performances and usability by a complete rewrite of most of the code. Since April 2018, he has been a part of the GReD s.r.l. team.

Mariarosaria Manzo was born in Naples, Italy, in 1973. She received the Laurea degree (*summa cum laude*) in mathematics from the University of Naples Federico II, Naples, Italy, and the Ph.D. degree in methods and technologies for environmental monitoring from the University of Basilicata, Potenza, Italy, in 1998 and 2008, respectively.

In 2002, she joined the Istituto per il Rilevamento Elettromagnetico dell'Ambiente (IREA), Italian National Research Council (CNR), Naples, Italy, where she is currently a Permanent Researcher. She was a Visiting Researcher with German Aerospace Center (DLR), Oberpfaffenhofen, Germany, in 2004, and with the Geodesy Laboratory, University of Miami, Coral Gables, FL, USA, in 2007. She has been and is currently involved in several national and international research projects. Her research interests include differential SAR interferometry (DInSAR) data processing and applications for the monitoring of surface displacements, such as those produced by subsidence, volcano activity, earthquakes, and landslides. Her current research interests also include the development of optimization/inversion algorithms for the analytical modeling of seismic and volcanic sources by using DInSAR and geodetic data.

Andrea Virgilio Monti-Guarnieri (Senior Member, IEEE) received the M.Sc. *cum laude* degree in electronic engineering in 1988.

Since 2017, he has been a Full Professor with the "Dipartimento di Elettronica, Informazione e Bioingegneria," Politecnico di Milano, Milano, Italy. He is the Founder of Polimi spin-off Aresys (2003), targeting SAR, radar, and geophysics applications. He is currently a Member of ESA GCLASS (HydroTerra) Mission Advisory Group. His H index (Google) is 32, with 4900 citations and applications for five patents. His current interest interests include radar-based system design, calibration and customized solution development, MIMO, and geosynchronous SAR.

Prof. Monti-Guarnieri was the recipient of four conference awards. He has been a Reviewer of many scientific journals, Guest Editor for MDPI *Remote Sensing*, and a Member of scientific technical committees of international workshops and symposia on radar and earth observation (EO).

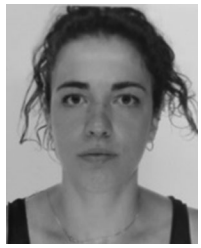

Federica Murgia received the Laurea (Doctor's) degree in telecommunication engineering (*cum laude*) and the Ph.D. degree in information and communication technologies (curriculum applied electromagnetics) from the University of Rome "La Sapienza," Rome, Italy, in 2016 and 2020, respectively.

During her Ph.D. studies, she has collaborated with the Istituto Nazionale di Geofisica e Vulcanologia (INGV), Rome, Italy. Her research interests include SAR data processing and analysis for ground deformation and atmospheric delay retrieval, time-series analysis for hazard monitoring, and microwave tomography image processing for GPR data analysis.

Eugenio Realini received the Ph.D. degree from the Politecnico di Milano, Milano, Italy, in 2009.

He cofounded and developed the open-source positioning software goGPS. In 2009, he received a JSPS Postdoctoral Fellowship with Osaka City University, Osaka, Japan, to integrate goGPS with open web-based GIS services. From 2011 to 2014, he was a Postdoctoral Researcher with Kyoto University, Kyoto, Japan, dealing with GNSS-based tropospheric monitoring and analysis for water vapor retrieval, also using low-cost receivers. Since 2014, he has been with Geomatics Research and Development srl, Lomazzo, Italy. His research interests include GNSS applications for positioning and earth sciences and the use of low-cost GNSS receivers.

Simona Verde received the M.S. degree (*summa cum laude*) in telecommunication engineering and the Ph.D. degree in information engineering from the University of Naples "Parthenope," Naples, Italy, in 2011 and 2015, respectively.

Since 2011, she has been collaborating with the National Research Council Institute for Electromagnetic Sensing of the Environment, Naples, Italy. In 2017, she was a Visiting Scientist with the Institute of Remote Sensing and Digital Earth (RADI), Chinese Academy of Sciences (CAS), Beijing, China. Her main research interests include spaceborne synthetic aperture radar (SAR) data processing, multibaseline DInSAR, and SAR tomography, with a special application focus on environmental and built monitoring.

Dr. Verde was the recipient of an award at the Joint Urban Remote Sensing Event Student Paper Competition, São Paulo, Brazil, in 2013.